Li, K., Ogden, R. W. and Holzapfel, G. A. (2018) A discrete fiber dispersion method for excluding fibers under compression in the modeling of fibrous tissues. Journal of the Royal Society: Interface, 15(138), 20170766.

There may be differences between this version and the published version. You are advised to consult the publisher's version if you wish to cite from it.

Deposited on: 2 February 2018

A Discrete Fiber Dispersion Method for Excluding Fibers under Compression in the Modeling of Fibrous Tissues

Kewei Li[1], Ray W. Ogden[2], and Gerhard A. Holzapfel[1,3] [†]

[1]Institute of Biomechanics, Graz University of Technology
Stremayrgasse 16-II, 8010 Graz, Austria

[2]School of Mathematics and Statistics, University of Glasgow
University Place, Glasgow G12 8SQ, Scotland, UK

[3]Faculty of Engineering Science and Technology,
Norwegian University of Science and Technology (NTNU), 7491 Trondheim, Norway

Abstract. Recently, micro-sphere based methods derived from the angular integration approach have been used for excluding fibers under compression in the modeling of soft biological tissues. However, recent studies have revealed that many of the widely used numerical integration schemes over the unit sphere are inaccurate for large deformation problems even without excluding fibers under compression. Thus, in this study, we propose a discrete fiber dispersion model based on a systematic method for discretizing a unit hemisphere into a finite number of elementary areas, such as spherical triangles. Over each elementary area we define a representative fiber direction and a discrete fiber density. Then, the strain energy of all the fibers distributed over each elementary area is approximated based on the deformation of the representative fiber direction weighted by the corresponding discrete fiber density. A summation of fiber contributions over all elementary areas then yields the resultant fiber strain energy. This treatment allows us to exclude fibers under compression in a discrete manner by evaluating the tension–compression status of the representative fiber directions only. We have implemented this model in a finite element program and illustrate it with three representative examples, including simple tension and simple shear of a unit cube, and non-homogeneous uniaxial extension of a rectangular strip. The results of all three examples are consistent and accurate compared with the previously developed continuous fiber dispersion model, and that is achieved with a substantial reduction of computational cost.

Keywords: Discrete fiber dispersion model; exclusion of compressed fibers; constitutive modeling; finite element analysis; fibrous tissue

---

[†]To whom correspondence should be addressed. Email address: `holzapfel@tugraz.at`

1 Introduction

Collagen fibers in soft biological tissues provide the overall stiffness and strength of the material. The latest imaging techniques, such as second-harmonic generation, have enabled detailed visualization of the underlying microscopic constitution of biological tissues such as arterial walls [1–3], carotid arteries [4], the myocardium [5, 6], the pericardium [7], articular cartilage [8, 9], and other tissues. The collagen fibers in these tissues may be dispersed randomly in space, in a certain pattern such as predominately in a particular direction [10], as a rotationally symmetric dispersion about a mean direction, or as the recently observed non-symmetric dispersion in arterial walls [1, 11], or other arrangements. Continuum constitutive laws that account for such underlying material micro-structure have been proposed and employed extensively in the last few decades to model the mechanical response of these fibrous tissues (see, e.g., [11–13]). In particular, constitutive laws that incorporate the three-dimensional (3D) fiber dispersion in fibrous tissues have attracted a lot of interest in the last decade. However, the precise description of the 3D fiber dispersion in a constitutive equation for the modeling of fibrous tissues poses formidable challenges even when considerable simplifications and idealizations are made.

Currently, there are two main approaches for modeling the dispersed fiber distributions in a constitutive equation, namely the 'generalized structure tensor' and the 'angular integration' (AI) approaches [11]. In the AI approach [14], the strain energy of a single collagen fiber is assumed to be a function of the fiber stretch. The fiber dispersion in the tissue is incorporated into the strain-energy function by an integration of the single fiber strain energy over all the fiber directions weighted with a continuous probability density function (PDF). Since the terminology 'angular integration' is rather imprecise and does not explicitly mention fiber dispersion, in the present paper instead of AI henceforth we use the terminology 'continuous fiber dispersion', abbreviated as CFD. If the fiber dispersion is incorporated as a summation of a finite number of discrete fiber contributions then we refer to this as the 'discrete fiber dispersion' (DFD) method.

The CFD approach has attracted a lot of interest, and since it was introduced in 1983 there have been numerous studies based on this approach; see [15] and references therein. Briefly, the fiber contribution Ψ_{f} to the strain-energy function of a tissue per unit reference volume is obtained by integrating the weighted strain energy $\Psi_n(\lambda)$ for each fiber direction $\mathbf{N}$ over the unit sphere $\mathbb{S}^2$, i.e.

$$\Psi_{\mathrm{f}} = \int_{\mathbb{S}^2} \rho(\mathbf{N})\Psi_n(\lambda)\,\mathrm{d}\Omega, \tag{1}$$

where λ is the fiber stretch in the direction $\mathbf{N}$, the PDF $\rho(\mathbf{N})$ represents the probability density

of the fiber in that direction in the reference configuration, and $\mathrm{d}\Omega$ is the solid angle on the sphere. Note that we are considering one fiber family of the same type embedded in the matrix material. The original study [14] allowed for different fibers to have different properties, but here we consider all the fibers to have the same properties. If additional fiber families of the same or different type exist in the tissue they can be included additively [16] with corresponding fiber volumetric ratios. The PDF in (1) must satisfy the normalization condition

$$\frac{1}{4\pi} \int_{\mathbb{S}^2} \rho(\mathbf{N})\,\mathrm{d}\Omega = 1. \tag{2}$$

The computational implementation of the CFD approach (1) requires two-dimensional integration over a unit sphere at each Gauss point during a finite element analysis. In general, due to the complex natures of ρ and Ψ_n, analytical solutions of the integration in (1) only exist for some special cases. Frequently, it is evaluated by numerical methods such as

$$\Psi_{\mathrm{f}} \approx \sum_{n=1}^{m} \rho(\mathbf{N}_n)\Psi_n(\lambda_n)w_n, \tag{3}$$

where $\mathbf{N}_n$ and w_n, respectively, for $n = 1, \ldots, m$, are integration points (orientations) and weights defined by the particular integration scheme over the unit sphere, m is the number of integration points, and λ_n, $n = 1, \ldots, m$, are the stretches associated with the integration points. In a recent study [17], large errors in the stress–strain result have been observed with some of the commonly used numerical integration schemes over the unit sphere, such as the method in [18]. The author of [17] concluded that the errors observed could be 'partially explained by the inability of standard methods to handle non-smooth functions even with a large number of integration points'. Out of the 20 numerical integration schemes over the unit sphere studied in [19], the best two integration schemes [18, 20] have been found to be inaccurate for large deformation problems in a more recent study [21].

The only integration scheme found to be accurate is the FM900 scheme [22] which involves 900 integration points. However, the authors only tested the integration scheme under uniaxial and biaxial extensions. It is unknown whether this integration scheme would work for more complex loading conditions. Furthermore, in this scheme a few integration points have negative weights [22]. In the extreme case, if only fibers at these integration points are under tension, then the micro-sphere based model would produce a negative stress even for fibers under tension. When the exclusion of compressed fibers is accounted for in finite element analyses [23], the integration error is even larger with low order integration schemes. Although the authors of [23] obtained a homogeneous stress distribution in the circumferential direction of the artery by using high order integration schemes with 368 or 600 integration points, it is still unknown

3

whether the tested high order integration schemes are accurate enough for other large deformation problems.

Due to the waviness and slenderness of the fibers, it is often assumed that they do not contribute to the strain energy of the tissue when loaded under compression [24]. To incorporate such tension–compression behavior of the fibers in the strain-energy function, $\Psi_n(\lambda_n)$ is often set to zero in (3) when the fiber stretch λ_n at a particular integration point $\mathbf{N}_n$ is less than one [23, 25]. Setting $\Psi_n(\lambda_n)$ to zero within a sub-domain of sphere renders some strain-energy functions or their derivatives discontinuous. However, existing numerical integration schemes are often proposed for continuous functions such as polynomials over the entire unit sphere, as in the widely used numerical integration schemes described in [20] and [18], which were proposed for polynomial functions of certain degrees. In addition, setting $\Psi_n(\lambda_n)$ to zero within a sub-domain of the sphere is equivalent to using some of the integration points and weights for numerical integration of a function over only its complement. This treatment is questionable because the accuracy of the integration scheme may not be maintained for polynomial functions up to a certain degree locally over a sub-domain. Besides, if a realistic PDF measured from experiment is adopted, for example [3], the integrand could become more complex, and it could even be a discontinuous function.

The computational cost for the numerical evaluation of the fiber contribution over a subset of the unit sphere could be substantially reduced by using a recently proposed general invariant [27] or by using parallel computing platforms such as OPENMP [28]. Besides using parallel computing techniques on a high performance computing cluster, another possibility for modeling the tension–compression behavior of fibers is to use the DFD approach, which could reduce computational time while maintaining accuracy, as shown in this study. Although it is not practical to count the actual number of fibers in a tissue, the concept of the DFD approach has already been applied in several areas. For example, a 3D DFD model with 30 fiber directions was proposed for the modeling of human skin [29], and a bivariate normal distribution was adopted to describe the fiber arrangement. With appropriate parameters the model was able to represent various fiber arrangements such as aligned fibers or rotationally symmetric fiber dispersions. Although only 30 fiber directions were determined by using the parameters of the bivariate normal distribution, the model was able to capture the fiber undulation and fiber compression–tension behavior of skin tissue under simple loading scenarios.

Similarly, a DFD model that consists of six weighted fiber bundles was proposed in [30], with all the fibers in each bundle oriented in the same direction. The volume fraction of fibers in each bundle was given by the weights. The six weights were then used as structure parameters

in the model fitting. The case of six equal weights represents a 3D uniform fiber dispersion. The strain energy of each fiber bundle was assumed to be a function of the fiber stretch in the bundle direction, and that of all the fibers was determined by a weighted summation of the contributions from all six fiber bundles. Any fiber bundle under compression can easily be excluded from the fiber contribution to the strain-energy function. Although only six fiber bundles appeared in the constitutive equation, the model was able to approximately capture the mechanical response of rabbit skin, porcine skin, porcine aortic valve cusp, and rat myocardial tissues. However, one limitation of this model, because of the discretization, is that the material response is not always isotropic even when the six weights are the same. To overcome this unphysical prediction, the authors improved the model by using a generalized strain invariant [31], and more recently by increasing the number of equally weighted fiber bundles [32] since the fitting of a large number of different weights is not practical.

In the present study, we propose a systematic approach for determining the discrete fiber density of each fiber bundle directly from the fiber PDF in a straightforward way. Briefly, we first discretize the unit hemisphere into a finite number of spherical triangles and then compute a representative fiber direction at the centroid of each spherical triangle. The discrete fiber density for each representative fiber direction is then determined by numerical integration of the continuous fiber PDF over the corresponding spherical triangle. With this treatment, we can easily incorporate the tension–compression behavior of the fibers over each spherical triangle. Through three numerical examples we demonstrate that the current model is able to accurately match predictions of the previously developed CFD model when compressed fibers are excluded, with a substantial reduction of computational cost.

The present paper is structured as follows. In Section 2 we present the continuum mechanical framework for the proposed DFD model, including the discretization scheme for the unit sphere, the strain-energy function, and the Cauchy stress and elasticity tensors for 3D fiber dispersions. In Section 3 we introduce the von Mises distribution for the PDF specialized to a rotationally symmetric dispersion for illustration. Next, we provide a guideline for the implementation of the proposed discretization scheme in a finite element program. Additionally, specific forms of the strain-energy function associated with the fibers are provided. The theory introduced in Sections 2 and 3 is then applied to several representative examples with the aim of demonstrating the efficacy and efficiency of the proposed model. Finally, Section 4 summarizes the proposed computational approach and suggests some future directions.

2 Discrete Fiber Dispersion Model

In this section, we briefly present the continuum mechanical framework for the proposed DFD model including kinematics, the strain-energy function, and the corresponding Cauchy stress and elasticity tensors, which are introduced in a decoupled form.

2.1 Kinematics

The deformation map $\mathbf{x} = \boldsymbol{\chi}(\mathbf{X})$ transforms a material point $\mathbf{X}$ in the stress-free reference configuration into a spatial point $\mathbf{x}$ in the deformed configuration. The deformation gradient is defined as $\mathbf{F}(\mathbf{X}) = \partial\boldsymbol{\chi}(\mathbf{X})/\partial\mathbf{X}$, and its determinant $J = \det\mathbf{F}(\mathbf{X}) > 0$ represents the local volume ratio at point $\mathbf{X}$, with $J \equiv 1$ for a strictly incompressible material. Following the multiplicative decomposition of the deformation gradient [33, 34], we decouple $\mathbf{F}$ into a volumetric (dilatational) part $J^{1/3}\mathbf{I}$ and an isochoric (distortional) part $\overline{\mathbf{F}} = J^{-1/3}\mathbf{F}$, with $\det\overline{\mathbf{F}} \equiv 1$. Based on $\mathbf{F}$ we define the right Cauchy–Green tensor as $\mathbf{C} = \mathbf{F}^{\mathrm{T}}\mathbf{F}$ and its isochoric counterpart as $\overline{\mathbf{C}} = \overline{\mathbf{F}}^{\mathrm{T}}\overline{\mathbf{F}}$, with the corresponding first invariants defined by

$$I_1 = \mathrm{tr}\,\mathbf{C}, \qquad \bar{I}_1 = \mathrm{tr}\,\overline{\mathbf{C}}, \tag{4}$$

respectively. Let $\mathbf{N}$ be a fixed vector in the reference configuration; then $\mathbf{C} : \mathbf{N} \otimes \mathbf{N}$, denoted I_4, represents the square of the stretch in the direction $\mathbf{N}$. Its isochoric counterpart is denoted $\bar{I}_4$. Hence,

$$I_4 = \mathbf{C} : \mathbf{N} \otimes \mathbf{N}, \qquad \bar{I}_4 = \overline{\mathbf{C}} : \mathbf{N} \otimes \mathbf{N}. \tag{5}$$

Let us now introduce unit Cartesian basis vectors $\mathbf{E}_1$, $\mathbf{E}_2$, $\mathbf{E}_3$ and then express $\mathbf{N}$ in terms of spherical polar angles Θ and Φ relative to $\mathbf{E}_1$, $\mathbf{E}_2$, $\mathbf{E}_3$ such that

$$\mathbf{N} = \sin\Theta\cos\Phi\mathbf{E}_1 + \sin\Theta\sin\Phi\mathbf{E}_2 + \cos\Theta\mathbf{E}_3. \tag{6}$$

2.2 Strain-energy Function

We assume that the 3D fiber dispersion inside the matrix material can be described by an integrable function $\rho(\mathbf{N})$, which we now write as $\rho(\Theta, \Phi)$, defined over the unit hemisphere

$$\mathbb{S} = \{(\Theta, \Phi) \mid \Theta \in [0, \pi], \Phi \in [0, \pi]\}. \tag{7}$$

Ideally, ρ should be determined by imaging analysis [3].

If the strain energy associated with an individual fiber direction $\mathbf{N}$ is described by a function $\Psi_n(I_4)$, where I_4 is defined in $(5)_1$, we require

$$\Psi_n(1) = 0, \qquad \Psi_n'(1) = 0, \tag{8}$$

and, following the CFD approach [35], the strain-energy function of all fibers in the reference configuration can be written over the unit hemisphere as

$$\Psi_f = \frac{1}{2\pi} \int_{\mathbb{S}} \rho(\Theta, \Phi) \Psi_n(I_4) \sin \Theta \, d\Theta \, d\Phi. \tag{9}$$

Inspired by the discrete nature of fibers dispersed within the ground matrix, and the fact that the number of fibers is finite, we may treat the fibers in a discrete manner. Ideally, the dispersion of fibers and the number of fibers should be determined by experimental measurement. However, due to the large number of fibers, their actual number and orientations at a specific point in the tissue may not be possible to determine accurately. Thus, in the present study we first discretize the unit hemisphere into a finite number of elementary areas $\Delta\mathbb{S}_n, n = 1, \ldots, m$. An example of such a discretization with spherical triangles is shown in Fig. 1(b). Note that only half of the representative fiber directions are needed because of symmetry. We then identify representative fiber angles (Θ_n, Φ_n) (associated with the centroids of the spherical triangles) for each elementary area and use these angles to represent all the fibers distributed within $\Delta\mathbb{S}_n$. Thus, the number of representative fiber angles is equal to the number of spherical triangles over the unit sphere, as can be seen in Figure 1. If the area of $\Delta\mathbb{S}_n$ is chosen to be very small, then the variation of the fiber directions within $\Delta\mathbb{S}_n$ becomes negligible. In the extreme case when $\Delta\mathbb{S}_n$ shrinks to a point, then the fiber direction is unique. The normalized number of fibers within each elementary area can then be determined from a set of m discrete fiber densities ρ_n defined by

$$\rho_n = \frac{1}{2\pi} \int_{\Delta\mathbb{S}_n} \rho(\Theta, \Phi) \sin \Theta \, d\Theta \, d\Phi, \qquad n = 1, \ldots, m. \tag{10}$$

In fact, $\rho(\Theta, \Phi)$ could be a discontinuous function over the hemisphere because the integration in (10) can be carried out over continuous sub-domains of the hemisphere. Similarly, the discrete fiber densities ρ_n satisfy the normalization condition over the unit hemisphere, i.e.

$$\sum_{n=1}^{m} \rho_n = 1, \tag{11}$$

which is the discrete counterpart of (2) on a hemisphere, where m denotes the number of representative fiber directions embedded in the matrix at a specific material point. The value of ρ_n depends on the area of $\Delta\mathbb{S}_n$ and the fiber dispersion. The areas of the $\Delta\mathbb{S}_n$s on the sphere can
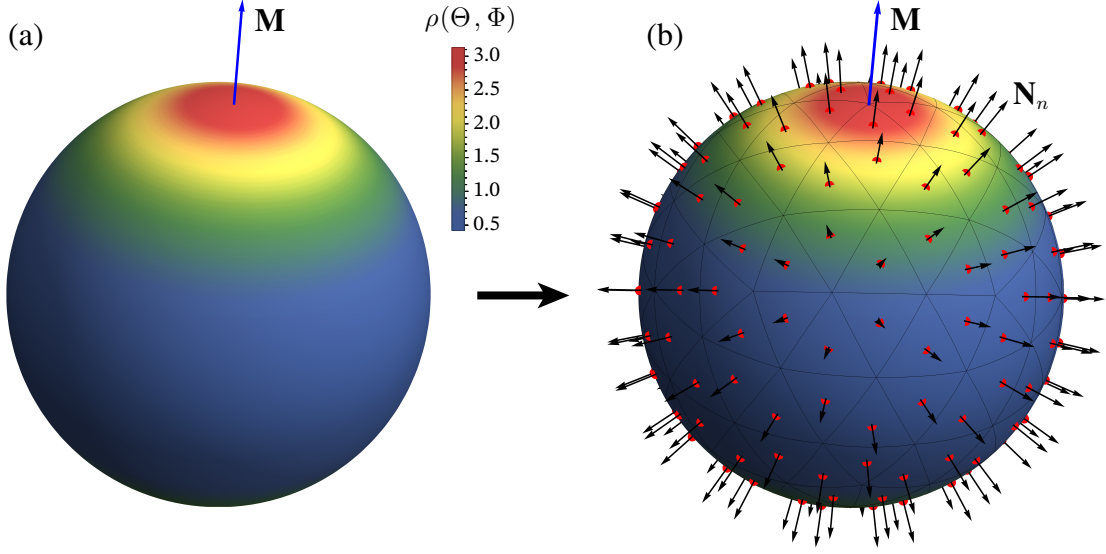
7

Figure 1: (a) Contour plot of the PDF $\rho(\Theta, \Phi)$ defined over the unit sphere by the von Mises distribution with mean fiber direction $\mathbf{M}$ and a concentration parameter $b = 1.0$, see (25); (b) example of a triangular discretization of the sphere with $2m$ representative fiber directions $\mathbf{N}_n$ (black arrows) defined at the centroids (red dots) of the spherical triangles.

vary or be nearly equal, as shown in Fig. 1(b). If necessary, regions with higher fiber density, for example, the region near the mean fiber direction $\mathbf{M}$ in Fig. 1(b), can be discretized with smaller $\Delta \mathbb{S}_n$. However, in this study, for the purpose of demonstration, we choose the triangular discretization shown in Fig. 1. With a discretized hemisphere, we then re-define the strain-energy function (9) for all the fiber contributions as

$$\Psi_{\mathrm{f}} = \sum_{n=1}^{m} \rho_n \Psi_n(I_{4n}), \tag{12}$$

where $I_{4n} = \mathbf{C} : \mathbf{N}_n \otimes \mathbf{N}_n$ and $\mathbf{N}_n$ is defined at the centroid of each spherical triangle via (6) with $\Theta = \Theta_n$ and $\Phi = \Phi_n$; see the black arrows in Fig. 1(b). Next, in order to exclude fibers under compression within a dispersion, we define Ψ_n as

$$\Psi_n(I_{4n}) = \begin{cases} f(I_{4n}) & \text{if } I_{4n} \geq 1 \\ 0 & \text{if } I_{4n} < 1. \end{cases} \tag{13}$$

A representative plot of the strain-energy function associated with one fiber versus I_{4n} is shown in Fig. 2. As can be seen, the strain energy is only non-zero when $I_{4n} > 1$. Note that the first derivative of the strain-energy function with respect to I_{4n} is continuous and equal to zero at $I_{4n} = 1$, and hence, with the requirement (8), $f(1) = f'(1) = 0$.
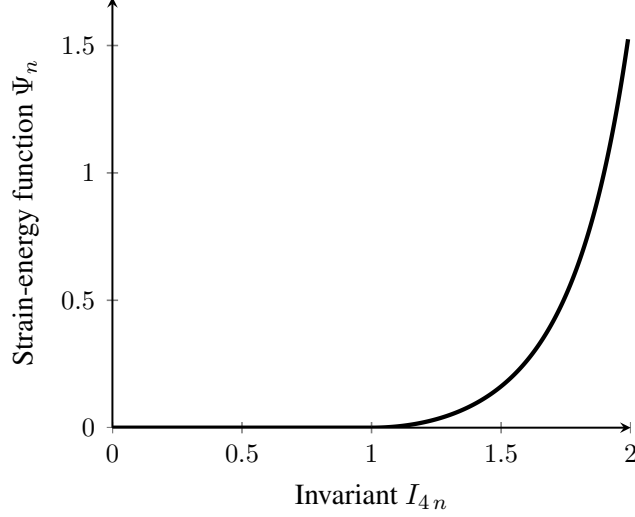
Figure 2: An example of a strain-energy function Ψ_n given by (13) associated with one fiber versus the invariant I_{4n}. Note that at $I_{4n} = 1$, $\Psi_n(1) = \Psi_n'(1) = 0$.

For efficient computational implementation, we write the strain-energy function in a decoupled form, namely $\Psi = \Psi_{\mathrm{vol}} + \Psi_{\mathrm{iso}}$, where Ψ_{vol} is the volumetric strain-energy function and Ψ_{iso} is the isochoric part of the strain-energy function associated with one family of embedded fibers, given by

$$\Psi_{\mathrm{iso}} = \Psi_{\mathrm{g}} + \Psi_{\mathrm{f}}, \tag{14}$$

where Ψ_{g} denotes the isochoric strain energy of the ground matrix, which is assumed to be isotropic and to depend only on $\bar{I}_1$. Then, from (12) and (14) we have

$$\Psi_{\mathrm{iso}} = \Psi_{\mathrm{g}}(\bar{I}_1) + \sum_{n=1}^{m} \rho_n \Psi_n(\bar{I}_{4n}), \quad \Psi_n(\bar{I}_{4n}) = \begin{cases} f(\bar{I}_{4n}) & \text{if } I_{4n} \geq 1 \\ 0 & \text{if } I_{4n} < 1, \end{cases} \tag{15}$$

where $\bar{I}_{4n} = \overline{\mathbf{C}} : \mathbf{N}_n \otimes \mathbf{N}_n$. For strictly incompressible materials we have $\lim_{J \to 1} \bar{I}_{4n} = I_{4n}$.

Since our focus is on incompressible materials, the volumetric strain-energy function is used as a penalty function, and it is convenient to adopt a form for Ψ_{vol} given in FEAP [36], i.e.

$$\Psi_{\mathrm{vol}} = \frac{K}{4}(J^2 - 1 - 2\ln J), \tag{16}$$

where K is a penalty parameter. The derivations of the volumetric parts of the stress and elasticity tensors are straightforward and have been well documented [12, 37]. Hence, in the following we only derive the isochoric parts of the stress and elasticity tensors.

9

2.3 Cauchy Stress Tensor

The so-called fictitious second Piola–Kirchhoff stress tensor $\overline{\mathbf{S}}$ is determined by differentiation of the isochoric strain-energy function with respect to $\overline{\mathbf{C}}/2$. Thus, from (15) we obtain

$$\overline{\mathbf{S}} = 2\frac{\partial \Psi_{\text{iso}}}{\partial \overline{\mathbf{C}}} = 2\psi_{\text{g}}'(\bar{I}_1)\mathbf{I} + 2\sum_{n=1}^{m} \rho_n \overline{\mathbf{S}}_n, \quad \overline{\mathbf{S}}_n = \begin{cases} f'(\bar{I}_{4n})\mathbf{N}_n \otimes \mathbf{N}_n & \text{if } I_{4n} \geq 1 \\ 0 & \text{if } I_{4n} < 1, \end{cases} \tag{17}$$

where $\mathbf{I}$ is the second-order unit tensor, $\psi_{\text{g}}'(\bar{I}_1) = \partial \Psi_{\text{g}}(\bar{I}_1)/\partial \bar{I}_1$, $f'(\bar{I}_{4n}) = \partial f(\bar{I}_{4n})/\partial \bar{I}_{4n}$, and $\bar{I}_1$ is given in (4)$_2$. Push-forward of $\overline{\mathbf{S}}$ yields the fictitious Cauchy stress tensor $\overline{\boldsymbol{\sigma}}$ as

$$\overline{\boldsymbol{\sigma}} = J^{-1}\overline{\mathbf{F}}\,\overline{\mathbf{S}}\,\overline{\mathbf{F}}^{\text{T}} = 2J^{-1}\left[\psi_{\text{g}}'(\bar{I}_1)\overline{\mathbf{b}} + \sum_{n=1}^{m} \rho_n \overline{\boldsymbol{\sigma}}_n\right], \quad \overline{\boldsymbol{\sigma}}_n = \begin{cases} f'(\bar{I}_{4n})\overline{\mathbf{n}}_n \otimes \overline{\mathbf{n}}_n & \text{if } I_{4n} \geq 1 \\ 0 & \text{if } I_{4n} < 1, \end{cases} \tag{18}$$

where $\overline{\mathbf{b}} = \overline{\mathbf{F}}\,\overline{\mathbf{F}}^{\text{T}}$ is the modified left Cauchy–Green tensor, and $\overline{\mathbf{n}}_n = \overline{\mathbf{F}}\mathbf{N}_n$. The isochoric Cauchy stress tensor $\boldsymbol{\sigma}_{\text{iso}}$ is then determined as

$$\boldsymbol{\sigma}_{\text{iso}} = \mathbb{P} : \overline{\boldsymbol{\sigma}}, \tag{19}$$

where $\mathbb{P} = \mathbb{I} - \frac{1}{3}\mathbf{I} \otimes \mathbf{I}$ is the fourth–order Eulerian projection tensor, and the symmetric fourth–order unit tensor $\mathbb{I}$ is defined in component form by $(\mathbb{I})_{abcd} = \frac{1}{2}(\delta_{ac}\delta_{bd} + \delta_{ad}\delta_{bc})$, where δ_{ad} is the Kronecker delta.

2.4 Elasticity Tensor

The fourth-order fictitious elasticity tensor $\overline{\mathbb{C}}$ in the Lagrangian description is obtained via differentiation of $\overline{\mathbf{S}}$ with respect to $\overline{\mathbf{C}}/2$ followed by multiplication by a factor $J^{-4/3}$. This, with (17), gives

$$\overline{\mathbb{C}} = 2J^{-4/3}\frac{\partial \overline{\mathbf{S}}}{\partial \overline{\mathbf{C}}} = 4J^{-4/3}\psi_{\text{g}}''(\bar{I}_1)\mathbf{I} \otimes \mathbf{I} + 4J^{-4/3}\sum_{n=1}^{m} \rho_n \overline{\mathbb{C}}_n,$$

$$\overline{\mathbb{C}}_n = \begin{cases} f''(\bar{I}_{4n})\mathbf{N}_n \otimes \mathbf{N}_n \otimes \mathbf{N}_n \otimes \mathbf{N}_n & \text{if } I_{4n} \geq 1 \\ 0 & \text{if } I_{4n} < 1, \end{cases} \tag{20}$$

where

$$\psi_{\text{g}}''(\bar{I}_1) = \frac{\partial^2 \Psi_{\text{g}}(\bar{I}_1)}{\partial \bar{I}_1 \partial \bar{I}_1}, \qquad f''\left(\bar{I}_{4n}\right) = \frac{\partial^2 f\left(\bar{I}_{4n}\right)}{\partial \bar{I}_{4n} \partial \bar{I}_{4n}}. \tag{21}$$

Note that for the neo-Hookean model, for which

$$\Psi_{\text{g}}(\bar{I}_1) = \frac{\mu}{2}(\bar{I}_1 - 3), \tag{22}$$

we have $\psi_g''(\bar{I}_1) = 0$, where the constant $\mu\,(>0)$ is the shear modulus. We adopt this model here because it has been shown in [38] that it is sufficient to use a neo-Hookean model for the ground matrix.

A push-forward operation of $\overline{\mathbb{C}}$ with $\mathbf{F}$ yields the fictitious elasticity tensor in the Eulerian description, i.e.

$$\overline{\mathbb{c}} = 4J^{-1}\sum_{n=1}^{m} \rho_n \overline{\mathbb{c}}_n, \quad \overline{\mathbb{c}}_n = \begin{cases} f''(\bar{I}_{4\,n})\overline{\mathbf{n}}_n \otimes \overline{\mathbf{n}}_n \otimes \overline{\mathbf{n}}_n \otimes \overline{\mathbf{n}}_n & \text{if } I_{4\,n} \geq 1 \\ 0 & \text{if } I_{4\,n} < 1, \end{cases} \tag{23}$$

where the neo-Hookean model has been used. If $\psi_g''(\bar{I}_1) \neq 0$, then an additional term should be included in $(23)_1$. Finally, with (23), we obtain the resulting isochoric part of the elasticity tensor in the Eulerian description, i.e.

$$\mathbb{c}_{\text{iso}} = \mathbb{P} : \bar{\mathbb{c}} : \mathbb{P} + \frac{2}{3}\text{tr}(\bar{\boldsymbol{\sigma}})\mathbb{P} - \frac{2}{3}(\boldsymbol{\sigma}_{\text{iso}} \otimes \mathbf{I} + \mathbf{I} \otimes \boldsymbol{\sigma}_{\text{iso}}), \tag{24}$$

which is needed for the finite element implementation together with the volumetric part [37].

3 Computational Aspects and Representative Examples

3.1 Choices of Fiber Distribution and Fiber Model

We have implemented the proposed DFD model (15) in the general purpose finite element analysis program FEAP [36] at the integration point level. Note that in the continuum mechanical framework described in Section 2 we have not specified any particular form of the fiber PDF $\rho(\Theta, \Phi)$. Thus, our model is applicable to any type of fiber dispersion, symmetric or non-symmetric. Here, for illustration of the method, we choose the rotationally symmetric fiber dispersion described by the von Mises distribution

$$\rho(\Theta, \Phi) = 4\sqrt{\frac{b}{2\pi}}\frac{\exp[2b(\mathbf{N} \cdot \mathbf{M})^2]}{\text{erfi}(\sqrt{2b})}, \tag{25}$$

where b is a concentration parameter describing how closely the fibers are distributed around the mean fiber direction $\mathbf{M}$, $\text{erfi}(x) = -\text{i}\,\text{erf}(\text{i}x)$ denotes the imaginary error function and $\text{erf}(x)$ is the standard error function. This distribution will be used in all the numerical examples.

On substituting (25) into (10), we obtain a set of m discrete fiber densities ρ_n for the representative fiber directions $\mathbf{N}_n$, $n = 1, \ldots, m$. A general guideline for discretizing the hemisphere and for determining the ρ_n is given in the accompanying box (Algorithm 1).

Algorithm 1: Discretization of the PDF $\rho(\Theta, \Phi)$

Data: input the mean fiber direction **M** and the PDF $\rho(\Theta, \Phi)$

Result: set of representative fiber directions $\mathbf{N}_n$ and associated densities ρ_n

begin

    set the dummy mean fiber direction as $\mathbf{M}_\mathrm{d}$ for $\Theta = \Phi = 0$

    define $\rho(\Theta, \Phi)$ with respect to $\mathbf{M}_\mathrm{d}$ via (25)

    compute the three vertices and $\mathbf{N}_n$ at the centroid of each spherical triangle with the code provided in Appendix A

    for each spherical triangle **do**

        compute the discrete fiber densities ρ_n by using the numerical integration rule of [39]

        rotate $\mathbf{N}_n$ to the corresponding location of the actual **M** by using Rodrigues' rotation formula [40]

    end

end

For the numerical examples, we also need to specify the single fiber strain-energy function $f(\bar{I}_4)$. For example, one possible choice is the exponential form $f(\bar{I}_4)$ proposed in [24] that can capture the highly nonlinear behavior of soft tissues, i.e.

$$f(\bar{I}_4) = \frac{k_1}{2k_2} \left\{ \exp[k_2(\bar{I}_4 - 1)^2] - 1 \right\}, \tag{26}$$

where k_1 is a positive material parameter with the dimension of stress, and k_2 is a positive dimensionless parameter. For comparison with existing results, we have also implemented the quadratic form (the standard fiber reinforcing model [41]) of $f(\bar{I}_4)$, i.e.

$$f(\bar{I}_4) = \frac{\nu}{2}(\bar{I}_4 - 1)^2, \tag{27}$$

where ν is a non-negative material constant with the dimension of stress. It is easy to verify that both relations (26) and (27) satisfy $f(1) = f'(1) = 0$, $f(\bar{I}_4) > 0$ and $f'(\bar{I}_4) > 0$ for $\bar{I}_4 > 1$. On substituting either (26) or (27) into the isochoric Cauchy stress tensor (19) and the Eulerian fictitious elasticity tensor (23), we obtain the specific forms of the Cauchy stress and Eulerian elasticity tensors.

3.2 Representative Numerical Examples

In order to illustrate the performance of the proposed DFD model we present three representative examples, specifically the homogeneous simple tension and simple shear of a unit cube with a 3D fiber dispersion, and the inhomogeneous extension of a rectangular strip with a mean fiber direction which does not coincide with the loading direction. For each of the three examples we assume that the material is incompressible. To enforce the incompressibility condition, we use the augmented Lagrangian method [42] in FEAP. In each example, the geometry of the model is discretized with 8–node hexahedral mixed Q1/P0 elements, and each problem is solved by using the Newton–Raphson method. The proposed model is implemented at the Gauss point level. During the finite element analysis, the frequency by which the stress and elasticity tensors is updated depends on the actual problem. The finite element solutions of the first two examples are verified by MATLAB or MATHEMATICA solutions [43, 44] based on analytical expressions obtained using the corresponding CFD model, as previously reported in [16]. The last example is verified by comparing with the numerical solution obtained by the CFD model, which is reported in [35].

3.2.1 Simple Tension

Here we consider a uniaxial tension test of an incompressible unit cube, as described in Section 3.1 of [16]. Briefly, we consider one family of fibers with a rotationally symmetric dispersion embedded in an isotropic matrix material. The mean fiber direction is taken to be aligned with the loading direction $\mathbf{E}_3$, as depicted in Fig. 3. Thus, only a subset of fibers around the mean fiber direction over the hemisphere and the mean fiber direction itself are under tension. The fibers under tension form a right circular cone [45], and the fibers outside the cone are under compression. We apply a displacement boundary condition on the top face of the unit cube to impose a stretch of 1.2, as indicated in Figure 3.

For this particular example, $I_4(\mathbf{N})$ for any fiber direction $\mathbf{N}$ is given by

$$I_4(\mathbf{N}) = \lambda^{-1} \sin^2 \Theta + \lambda^2 \cos^2 \Theta, \tag{28}$$

where λ is the fiber stretch in the loading direction. Note that $I_4(\mathbf{N})$ is independent of Φ in this special case. The general form of the Cauchy stress tensor $\boldsymbol{\sigma}$ for this problem is given by [16]

$$\boldsymbol{\sigma} = -p\mathbf{I} + \mu\mathbf{b} + \frac{k_1}{\pi} \int_\Omega \rho(\Theta, \Phi) \exp[k_2(I_4 - 1)^2](I_4 - 1) \sin \Theta \, \mathbf{n} \otimes \mathbf{n} \, \mathrm{d}\Theta \, \mathrm{d}\Phi, \tag{29}$$

where for this special case we define the integration domain as $\Omega = \{(\Theta, \Phi) \mid \Theta \in [0, \pi/2], \Phi \in [0, 2\pi], I_4 > 1\}$, p is the Lagrange multiplier, $\mathbf{n} = \mathbf{FN}$, and, because of symmetry, the PDF
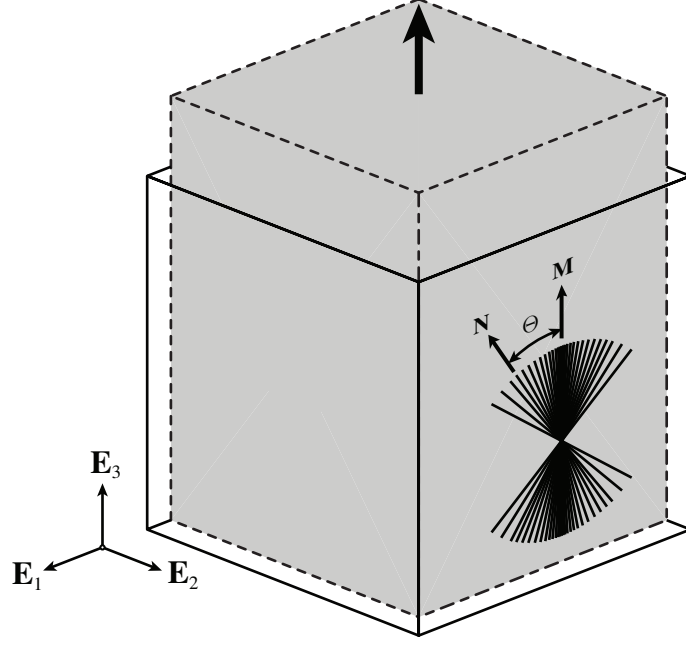
Figure 3: Deformation of a unit cube under simple tension. Rotationally symmetric fiber dispersion with the mean fiber direction **M** aligned along the loading direction $\mathbf{E}_3$ in the reference configuration (solid lines). An arbitrary fiber direction within the dispersion is denoted by **N**. The fiber dispersion is 3D but only a cross-section in the $(\mathbf{E}_1, \mathbf{E}_3)$-plane is shown. The dashed lines refer to the deformed configuration of the cube, shown in gray, at a stretch of 1.2.

$\rho(\Theta, \Phi)$ reduces to

$$\rho(\Theta) = 4\sqrt{\frac{b}{2\pi}} \frac{\exp(2b\cos^2\Theta)}{\mathrm{erfi}(\sqrt{2b})}. \tag{30}$$

As given in [16], the uniaxial Cauchy stress $\sigma \equiv \sigma_{33}$ in the loading direction $\mathbf{E}_3$ is

$$\sigma = (\mu + \alpha)\lambda^2 - (\mu + \beta)\lambda^{-1}, \tag{31}$$

where α and β are defined over the domain $\Sigma = \{\Theta \in [0, \pi/2] \mid I_4 > 1\}$ as

$$\begin{aligned}
\alpha &= 2k_1 \int_\Sigma \rho(\Theta) \exp[k_2(I_4 - 1)^2](I_4 - 1)\sin\Theta\cos^2\Theta\,\mathrm{d}\Theta, \\
\beta &= k_1 \int_\Sigma \rho(\Theta) \exp[k_2(I_4 - 1)^2](I_4 - 1)\sin^3\Theta\,\mathrm{d}\Theta.
\end{aligned} \tag{32}$$

The Cauchy stress-stretch result (31) was implemented in MATLAB, and we obtained solutions of this problem with material parameters $\mu = 1.64\,\mathrm{kPa}$, $k_1 = 5.63\,\mathrm{kPa}$ and $k_2 = 14.25$ [16]. The relationship between the Cauchy stress and the stretch in the loading direction is shown in Fig. 4 for $b = 0.01$ and $b = 5$ (solid curves). For comparison we have also plotted the finite element solutions (open circles) by using the proposed DFD model in FEAP with the same
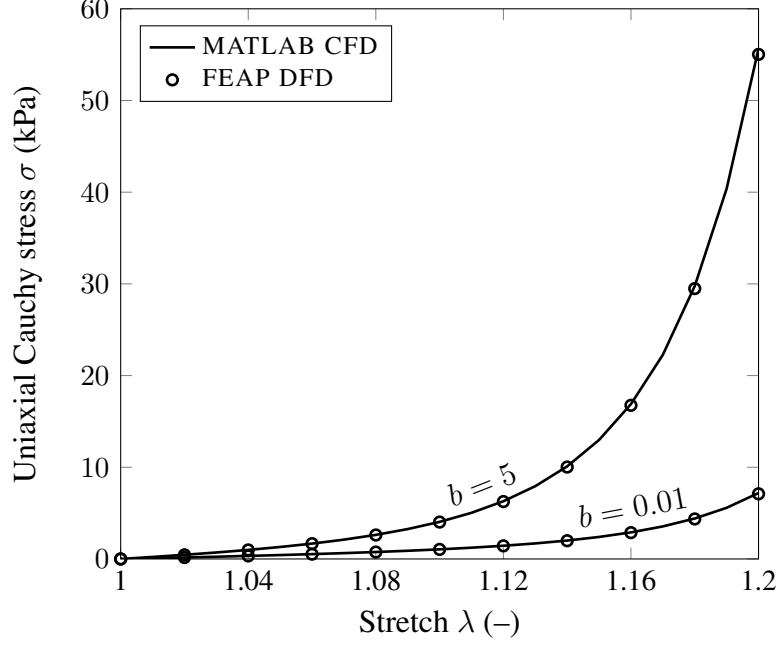
14

Figure 4: Comparison of the solutions of a simple tension test, obtained by using the previously developed CFD model [16] in MATLAB, and the finite element solutions obtained by using the proposed DFD model in FEAP with $m = 640$ discrete fiber directions. The material parameters $\mu = 1.64\,\text{kPa}$, $k_1 = 5.63\,\text{kPa}$, and $k_2 = 14.25$, and the values $b = 0.01$ and $b = 5$ of the concentration parameter were used in each case.

material parameters as in our previous study, and with $m = 640$ discrete fiber directions, which is enough to obtain very accurate results; see Figure 4. Note that the implementation of the proposed model in FEAP is based on the continuum mechanical framework of Section 2. As can be seen in Fig. 4, a very good match between the MATLAB and the finite element solutions for different concentration parameters has been obtained. This indicates that the DFD model is able to predict the same result as the CFD model for this particular problem.

Remark. For reason of completeness we now address the numerical results obtained by using the micro-sphere based approach. We rewrite the coefficients α and β in (31) over a subset of the whole unit sphere, i.e. $\Omega = \{(\Theta, \Phi) \mid \Theta \in [0, \pi], \Phi \in [0, 2\pi], I_4 > 1\}$. Thus,

$$
\begin{aligned}
\alpha &= \frac{k_1}{2\pi} \int_\Omega \rho(\Theta) \exp[k_2 (I_4 - 1)^2] (I_4 - 1) \cos^2 \Theta \, \mathrm{d}\Omega, \\
\beta &= \frac{k_1}{2\pi} \int_\Omega \rho(\Theta) \exp[k_2 (I_4 - 1)^2] (I_4 - 1) \sin^2 \Theta \cos^2 \Phi \, \mathrm{d}\Omega.
\end{aligned}
\tag{33}
$$

We then adopt the numerical integration scheme FM900 of [22] with 900 integration points, as discussed in [19]. To exclude fibers under compression, we only use the angles (Θ_i, Φ_i) and

weights w_i of the FM900 scheme if the fiber stretches in those directions are greater than one. Thus,

$$
\begin{aligned}
\alpha &\approx \frac{k_1}{2\pi} \sum_{i \in \omega} \rho(\Theta_i) \exp[k_2(I_4(\Theta_i) - 1)^2](I_4(\Theta_i) - 1)w_i \cos^2 \Theta_i, \\
\beta &\approx \frac{k_1}{2\pi} \sum_{i \in \omega} \rho(\Theta_i) \exp[k_2(I_4(\Theta_i) - 1)^2](I_4(\Theta_i) - 1)w_i \sin^2 \Theta_i \cos^2 \Phi_i,
\end{aligned}
\tag{34}
$$

where ω represents the set of angles that lie inside Ω. We have carried out the numerical integration in MATLAB and obtained the results for the Cauchy stress versus stretch with the concentration parameters $b = 5$ and 0.01. The relative error of the numerical result obtained by using the micro-sphere based approach (34) with the FM900 integration scheme [22] is small compared with the MATLAB solution based on the CFD model [16]. However, the numerical integration scheme with 21 points used in [18] is not able to reproduce the curves in Fig. 4. Similar results for the uniaxial and biaxial tension tests have also been observed for the case when the compressed fibers are not excluded [21]. Further numerical investigations are needed to verify whether this integration scheme is applicable in a finite element analysis with complex loading conditions. ∎

3.2.2 Simple Shear

Similarly to the previous section, here we test the capability and efficiency of the proposed DFD model by subjecting the same unit cube to a simple shear deformation, as described in [16]. Briefly, with reference to Fig. 5, all the nodes on the bottom face of the cube in the $(\mathbf{E}_1, \mathbf{E}_2)$-plane are constrained in all three translational degrees of freedom, and a horizontal displacement in the $\mathbf{E}_1$ direction is applied on the top face. We take the mean fiber direction $\mathbf{M}$ to be at $135°$ clockwise from the $\mathbf{E}_3$ direction in the $(\mathbf{E}_1, \mathbf{E}_3)$-plane in the reference configuration, as illustrated on a cross-section of the cube in Fig. 5. This orientation was chosen so that the exclusion of fibers under compression has a significant influence on the resulting shear stress.

The Cauchy shear stress component σ_{13} in the $(\mathbf{E}_1, \mathbf{E}_3)$-plane is given by [16]

$$
\sigma_{13} = (\mu + \alpha)c + \gamma,
\tag{35}
$$

where α and γ are defined by

$$
\begin{aligned}
\alpha &= \frac{k_1}{\pi} \int_\Omega \rho(\Theta, \Phi)(I_4 - 1) \exp\left[k_2(I_4 - 1)^2\right] \sin \Theta \cos^2 \Theta \, d\Theta \, d\Phi, \\
\gamma &= \frac{k_1}{\pi} \int_\Omega \rho(\Theta, \Phi)(I_4 - 1) \exp\left[k_2(I_4 - 1)^2\right] \sin^2 \Theta \cos \Theta \cos \Phi \, d\Theta \, d\Phi,
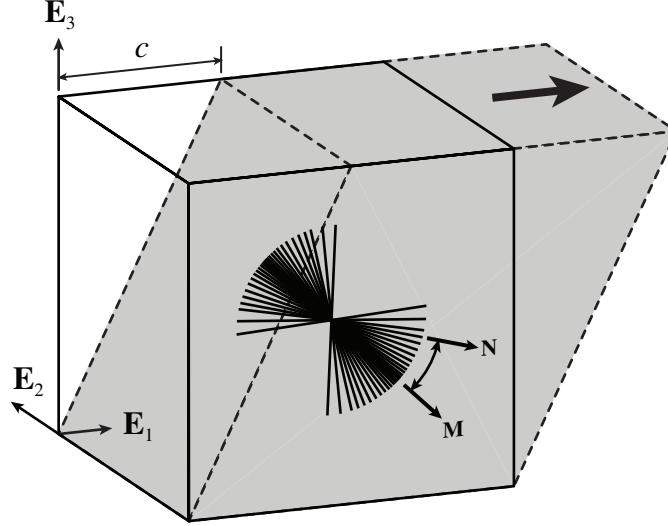\end{aligned}
\tag{36}
$$

16

Figure 5: Deformation of a unit cube under simple shear in the $(\mathbf{E}_1, \mathbf{E}_3)$-plane. The mean fiber direction $\mathbf{M}$ is aligned at $135°$ clockwise from the $\mathbf{E}_3$ direction in the reference configuration (solid lines). The 3D fiber dispersion is rotationally symmetric about $\mathbf{M}$, although only a cross-section in the $(\mathbf{E}_1, \mathbf{E}_3)$-plane is shown. The unit vector $\mathbf{N}$ in that cross-section represents a general fiber direction. The dashed lines refer to the deformed configuration of the cube, shown in gray, with an amount of shear $c = 0.5$.

and $\Omega = \{(\Theta, \Phi) \in \mathbb{S} \mid I_4 > 1\}$. For this particular example, the invariant $I_4(\mathbf{N})$ has the explicit form

$$I_4 = 1 + c^2 \cos^2 \Theta + c \sin 2\Theta \cos \Phi. \tag{37}$$

We implemented the result (35) in MATHEMATICA and obtained the solution for σ_{13} as a function of the amount of shear c. For this problem we used the parameters $\mu = 7.64\,\text{kPa}$, $b = 1.08$, $k_1 = 996.6\,\text{kPa}$, and $k_2 = 5.249$ [16]. For comparison we have also computed the case for $b = 2$. In Fig. 6 we have plotted the solutions from [16] and the numerical results by using the proposed DFD model with the same material parameters as in our previous study and with $m = 640$ discrete fiber directions. As can be seen, the numerical results match very well with the corresponding results from [16]. For higher values of m we obtained the same stress response, but for smaller values of m the prediction of the stress response became less accurate.
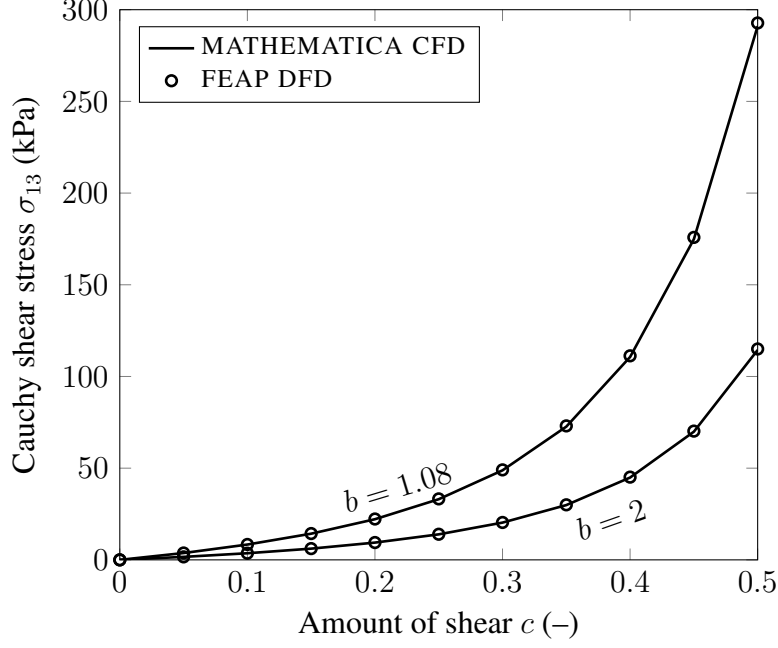
Figure 6: Comparison of the MATHEMATICA solutions obtained by the CFD model [16] and the finite element solutions obtained by the proposed DFD model with $m = 640$ for the simple shear of a unit cube. The material parameters are $\mu = 7.64\,\text{kPa}$, $k_1 = 996.6\,\text{kPa}$, and $k_2 = 5.249$, and the concentration parameters are $b = 1.08$ and 2.

3.3 Extension of a Rectangular Strip

In the previous two sections, we have verified the proposed DFD model with a unit cube under simple tension and simple shear. In the present example, we consider the uniaxial extension of a rectangular strip with loading direction different from the mean fiber direction. For this problem the deformation field is non-homogeneous, as distinct from the two previous examples. We choose this example because a solution of this problem obtained by using the corresponding CFD model has already been presented in [35]. Hence, we compare the results of the proposed DFD model with the existing results of the CFD model.

The geometry, the boundary conditions, and the 3D fiber dispersion of the rectangular strip are described in [35]. However, here we align the longitudinal direction with the $\mathbf{E}_3$ axis instead of the $\mathbf{E}_1$ axis, as shown in Fig. 7. Briefly, a rectangular strip of $10 \times 4 \times 1\,\text{mm}$ is discretized with 320 hexahedral elements. All nodes on the bottom face of the strip are constrained in the $\mathbf{E}_3$ direction. In addition, to prevent rigid body translation, we constrained the center node of the bottom face in the $\mathbf{E}_1$ and $\mathbf{E}_2$ directions. Furthermore, the $\mathbf{E}_2$ degree of freedom at node A on the bottom face of the strip, see Fig. 7(b), is also constrained to prevent rigid body rotation about the $\mathbf{E}_3$ axis. A 3D rotationally symmetric fiber dispersion is assumed with the mean
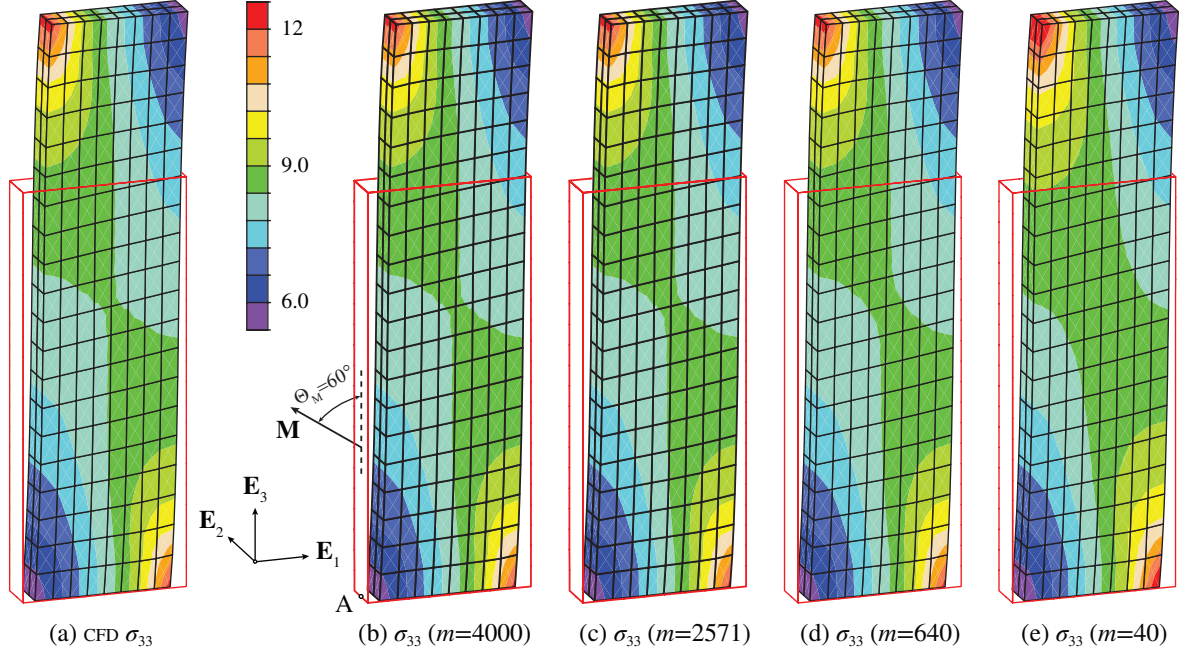
Figure 7: Comparison of the σ_{33} component of the Cauchy stress (kPa) distribution obtained by using (a) the CFD model [35], and the DFD model with discretization densities (b) $m = 4000$, (c) $m = 2571$, (d) $m = 640$ and (e) $m = 40$ for the uniaxial extension test of a rectangular strip at an axial stretch of $\lambda = 1.4$ with parameters $\mu = 5\,\mathrm{kPa}$, $\nu = 10\,\mathrm{kPa}$ and $b = 2.9$. We assumed a 3D rotationally symmetric fiber dispersion with a mean fiber direction **M** aligned at $\Theta_\mathrm{M} = 60°$ counterclockwise from the $\mathbf{E}_3$ axis in the $(\mathbf{E}_1, \mathbf{E}_3)$-plane.

fiber direction aligned at $60°$ from the $\mathbf{E}_3$ direction counterclockwise in the $(\mathbf{E}_1, \mathbf{E}_3)$-plane, see Fig. 7(b). A displacement boundary condition is applied on the top face of the strip to impose a stretch of $\lambda = 1.4$ in the $\mathbf{E}_3$ direction.

The numerical result for this problem obtained by using the CFD model with the quadratic fiber strain-energy function (27) has been provided in Section 4.2.1 of [35], and is reproduced here in Fig. 7(a). In Fig. 7(b)–(e), for comparison, the distributions of the Cauchy stress component σ_{33} in the deformed configuration obtained by using the DFD model with different values of m are also plotted. As can be seen, the numerical result by the DFD model approaches that of the CFD model as m increases. As shown in Fig. 7(b), the DFD result is essentially identical to the CFD result for $m = 4000$. This shows that we are able to approach the result of the CFD model with the proposed DFD model even when exclusion of compressed fibers is considered.

An important advantage of the DFD model is the substantial reduction in processing time. For example, the numerical simulation with the CFD model was completed in 3.3 hours on a typical Windows computer with an Intel® Core™ i7-4770 Processor and $16\,\mathrm{GB}$ of memory.

With the proposed DFD model, and a discretization density of $m = 4000$, the same problem was computed in only 53 seconds – a speedup of 224! Certainly, a further reduction of the processing time can be achieved with a smaller value of m, but the accuracy would then be reduced.

4   Concluding Remarks

In the present study we have proposed an efficient discrete fiber dispersion model capable of excluding fibers under compression in the modeling of the nonlinear behavior of fibrous tissues. We have introduced a systematic approach for discretizing the unit sphere into a finite number of spherical triangles and for computing the discrete fiber densities over each elementary spherical triangle. The discrete fiber densities associated with each spherical triangle are analogous to the weighting factors used in the micro-sphere based approach but have a direct physical meaning. We were then able to conceive of and formulate a strain-energy function in terms of contributions from each fiber bundle distributed within the corresponding spherical triangle. This discrete treatment of fiber contributions, inspired by the discrete nature of fibers embedded in fibrous tissues, allows us to exclude any fibers under compression within a 3D dispersion in a rather straightforward way. The resulting nonlinear elastic constitutive model depends only on those fiber bundles under tension as well as the matrix material under arbitrary 3D finite deformations.

With a volumetric/isochoric split of the deformation gradient we presented analytical expressions of the corresponding Cauchy stress and elasticity tensors in decoupled forms especially suitable for finite element implementation. By using the augmented Lagrangian method for enforcing material incompressibility and a mixed finite element formulation in FEAP, we have demonstrated the capability and efficiency of the proposed DFD model with three representative examples. For each of these examples we have observed very good agreement between the discrete model and the previously developed continuous model [16, 35]. The results indicate that the capability of the discrete model is equivalent to that of the continuous model when excluding fibers under compression but with a substantial computational speedup.

For demonstration purposes, we discretized the unit sphere simply with spherical triangles. Future studies on the optimization of the discretization scheme may include non-uniform or locally refined discretizations. In addition, we have tested the proposed model with a rotationally symmetric fiber dispersion. It is straightforward to implement other types of fiber arrangements such as the recently observed non-symmetric fiber dispersion [11]. The only part that needs

to be changed is the computation of the discrete fiber densities over each spherical triangle via numerical integration (Algorithm 1). The remaining part of the implementation is the same.

Compared with the micro-sphere based method, the proposed DFD model has several advantages.

- In the DFD model dispersed fibers are treated in a discrete manner, as they would occur naturally. For example, Fig. 7(e) shows the result of a rectangular strip with 40 discrete fiber bundles under uniaxial stretch. This result would then be exact for such a real fiber arrangement. On the other hand in the micro-sphere based method the dispersed fibers are considered to be continuously distributed. But their contribution is approximated by a numerical integration scheme, in which case the method is only valid for the functions for which the scheme was originally proposed. By contrast, the DFD method is independent of such numerical integration schemes, and any mechanical and failure properties of the fibers can be defined locally for each elementary area. If the representative fiber direction $\mathbf{N}_n$ is under compression, then all the fibers within $\Delta\mathbb{S}_n$ can be excluded.

- The discretization scheme used in the DFD method can be locally refined in a straightforward way as, for example, in [46]. When fibers are concentrated in several particular areas on a unit hemisphere, then the corresponding spherical triangles can be further divided into smaller ones to account for such locally concentrated fiber dispersions. However, if a micro-sphere based method is used, it may not be possible to add additional integration points locally within a sub-domain of the unit hemisphere.

- Within each elementary area (spherical triangle) the discrete fiber density ρ_n is evaluated by using a large number of $\rho(\Theta, \Phi)$ values, whereas in the micro-sphere based method $\rho(\Theta, \Phi)$ is evaluated at a single integration point. Thus, the DFD model uses more $\rho(\Theta, \Phi)$ information.

- In the DFD model the discrete fiber densities are computed by using a simple numerical integration scheme over the spherical triangles [39], and this integration is easy to perform because the variation of $\rho(\Theta, \Phi)$ over an elementary area is usually small. However, in the micro-sphere based method the computation of the integration points over the unit sphere, and the associated weights of a particular integration scheme could be very complex or even impossible to perform by users.

A future comparison study of the two methods with locally concentrated fibers, as documented in [3], and various loading conditions will provide more insight into their relative performance.

As shown in the example of Section 3.3, the DFD solution approaches that of the CFD model as the discretization number m increases. With increasing m the solution of the DFD model should theoretically approach the result of the CFD model for any problem. However, for larger m, the computational cost is higher. Thus, one aim when using the DFD model is to seek a balance between accuracy and computational efficiency. Certainly, we believe that the potential of this novel discrete model is far beyond its capability for excluding the compressed fibers that was demonstrated in the representative examples. The DFD model enables us to 'fine tune' the mechanical behavior and failure properties of any fiber orientation at any point within the tissue. Future studies on the modeling of fiber recruitment and anisotropic fiber damage with the DFD model will demonstrate the further potential of the approach presented here.

Appendix A: MATHEMATICA Code for Discretization of a Unit Sphere

We have written a MATHEMATICA code that was used for the discretization of the unit sphere into a finite number of spherical triangles, and we have tested the code in MATHEMATICA 11.0 on a Windows machine. Thereby the number of spherical triangles can be increased by increasing the number '2' in the definition of gridFaces in the following code.

```
$PreRead = (# /. s_String /; StringMatchQ[s, NumberString] &&
Precision@ToExpression@s == MachinePrecision :> s <> "`17." &);
<< PolyhedronOperations`
Quiet@Needs["VectorAnalysis`"]
gridFaces = Cases[Normal@Geodesate[PolyhedronData["Icosahedron"], 2,
{0, 0, 0}, 1.0], _Polygon, Infinity];
Mappg = CoordinateTransformData["Cartesian" -> "Spherical", "Mapping"];
Mg [vr_] = CoordinatesFromCartesian[vr, Spherical];
Grid[Table[
   Flatten[{Mg[Partition[gridFaces[[i, 1]], 3][[1]][[1]]][[2 ;; 3]],
     Mg[Partition[gridFaces[[i, 1]], 3][[1]][[2]]][[2 ;; 3]],
     Mg[Partition[gridFaces[[i, 1]], 3][[1]][[3]]][[2 ;; 3]],
     Normalize[RegionCentroid[ gridFaces[[i]] ]]}], {i,
   Length[gridFaces]}] , ItemStyle -> "Text" ];
NumberForm[N[%, 16], {17, 8}, NumberFormat -> (#1 &)]
```

For each spherical triangle, this program outputs the spherical coordinates of the three vertices in radians and the three Cartesian coordinates of its centroid in one row. Note that similar algorithms are also available for MATLAB, see, for example, [47].

References

[1] A. J. Schriefl, G. Zeindlinger, D. M. Pierce, P. Regitnig, and G. A. Holzapfel. Determination of the layer-specific distributed collagen fiber orientations in human thoracic and abdominal aortas and common iliac arteries. *J. R. Soc. Interface*, 9:1275–1286, 2012.

[2] A. J. Schriefl, H. Wolinski, P. Regitnig, S. D. Kohlwein, and G. A. Holzapfel. An automated approach for 3D quantification of fibrillar structures in optically cleared soft biological tissues. *J. R. Soc. Interface*, 10:20120760, 2013.

[3] J. A. Niestrawska, Ch. Viertler, P. Regitnig, T. U. Cohnert, G. Sommer, and G. A. Holzapfel. Microstructure and mechanics of healthy and aneurysmatic abdominal aortas: experimental analysis and modeling. *J. R. Soc. Interface*, 13:20160620, 2016.

[4] L. Azinfar, M. Ravanfar, Y. Wang, K. Zhang, D. Duan, and G. Yao. High resolution imaging of the fibrous microstructure in bovine common carotid artery using optical polarization tractography. *J. Biophotonics*, 10:231–241, 2017.

[5] W. J. Karlon, J. W. Covell, A. D. McCulloch, J. J. Hunter, and J. H. Omens. Automated measurement of myofiber disarray in transgenic mice with ventricular expression of ras. *Anat. Rec.*, 252:612–625, 1998.

[6] J. W. Covell. Tissue structure and ventricular wall mechanics. *Circulation*, 118:699–701, 2008.

[7] M. S. Sacks. Biomechanics of native and engineered heart valve tissues. In F. Guilak, D. L. Butler, St. A. Goldstein, and D. J. Mooney, editors, *Functional Tissue Engineering*, pages 243–257, New York, 2003. Springer-Verlag.

[8] M. B. Lilledahl, D. M. Pierce, T. Ricken, G. A. Holzapfel, and C. de Lange Davies. Structural analysis of articular cartilage using multiphoton microscopy: input for biomechanical modeling. *IEEE Trans. Med. Imaging*, 30:1635–1648, 2011.

[9] G. A. Ateshian, V. Rajan, N. O. Chahine, C. E. Canal, and C. T. Hung. Modeling the matrix of articular cartilage using a continuous fiber angular distribution predicts many observed phenomena. *J. Biomech. Eng.*, 131:61003, 2009.

[10] K. Zuo, T. Pham, K. Li, C. Martin, Z. He, and W. Sun. Characterization of biomechanical properties of aged human and ovine mitral valve chordae tendineae. *J. Mech. Behav. Biomed. uMater.*, 62:607–618, 2016.

[11] G. A. Holzapfel, J. A. Niestrawska, R. W. Ogden, A. J. Reinisch, and A. J. Schriefl. Modelling non-symmetric collagen fibre dispersion in arterial walls. *J. R. Soc. Interface*, 12:20150188, 2015.

[12] T. C. Gasser, R. W. Ogden, and G. A. Holzapfel. Hyperelastic modelling of arterial layers with distributed collagen fibre orientations. *J. R. Soc. Interface*, 3:15–35, 2006.

[13] G. A. Holzapfel and R. W. Ogden. Constitutive modelling of arteries. *Proc. R. Soc. Lond. A*, 466:1551–1597, 2010.

[14] Y. Lanir. Constitutive equations for fibrous connective tissues. *J. Biomech.*, 16:1–12, 1983.

[15] G. A. Holzapfel and R. W. Ogden. On the tension–compression switch in soft fibrous solids. *Eur. J. Mech. A/Solids*, 49:561–569, 2015.

[16] K. Li, R. W. Ogden, and G. A. Holzapfel. An exponential constitutive model excluding fibers under compression: application to extension-inflation of a residually stressed carotid artery. *Math. Mech. Solids.* in press.

[17] E. Verron. Questioning numerical integration methods for microsphere (and microplane) constitutive equations. *Mech. Mat.*, 89:216–228, 2015.

[18] Z. P. Bažant and B. H. Oh. Efficient numerical integration on the surface of a sphere. *Z. Angew. Math. Mech.*, 66:37–49, 1986.

[19] A. E. Ehret, M. Itskov, and H. Schmid. Numerical integration on the sphere and its effect on the material symmetry of constitutive equations–a comparative study. *Int. J. Numer. Meth. Engng*, 81:189–206, 2010.

[20] S. Heo and Y. Xu. Constructing fully symmetric cubature formulae for the sphere. *Math. Comp.*, 70:269–279, 2001.

24

[21] M. Itskov. On the accuracy of numerical integration over the unit sphere applied to full network models. *Comput. Mech.*, 57:859–865, 2016.

[22] J. Fliege and U. Maier. The distribution of points on the sphere and corresponding cubature formulae. *IMA J. Numer. Anal.*, 19:317–334, 1999.

[23] V. Alastrué, M. A. Martinez, M. Doblaré, and A. Menzel. Anisotropic micro–sphere–based finite elasticity applied to blood vessel modelling. *J. Mech. Phys. Solids*, 57:178–203, 2009.

[24] G. A. Holzapfel, T. C. Gasser, and R. W. Ogden. A new constitutive framework for arterial wall mechanics and a comparative study of material models. *J. Elasticity*, 61:1–48, 2000.

[25] P. Sáez, A. García, E. Peña, T. C. Gasser, and M. A. Martíne. Microstructural quantification of collagen fiber orientations and its integration in constitutive modeling of the porcine carotid artery. *Acta Biomater.*, 33:183–193, 2016.

[26] S. Federico and T. C. Gasser. Nonlinear elasticity of biological tissues with statistical fibre orientation. *J. R. Soc. Interface*, 7:955–966, 2010.

[27] K. Li, R. W. Ogden, and G. A. Holzapfel. Modeling of fibrous biological tissues with a general invariant that excludes compressed fibers. *J. Mech. Phys. Solids*, 110:38–53, 2018.

[28] R. Chandra, R. Menon, L. Dagum, D. Kohr, D. Maydan, and J. McDonald. *Parallel Programming in OpenMP*. Morgan Kaufmann, 2000.

[29] J. W. Y. Jor, M. P. Nash, P. M. F. Nielsen, and P. J. Hunter. Modelling the mechanical properties of human skin: towards a 3D discrete fibre model. *2007 29th Annual International Conference of the IEEE Engineering in Medicine and Biology Society*, pages 6640–6643, 2007.

[30] C. Flynn, M. B. Rubin, and P. Nielsen. A model for the anisotropic response of fibrous soft tissues using six discrete fibre bundles. *Int. J. Numer. Method Biomed. Eng.*, 27:1793–1811, 2011.

[31] C. Flynn and M. B. Rubin. An anisotropic discrete fibre model based on a generalised strain invariant with application to soft biological tissues. *Int. J. Eng. Sci.*, 60:66–76, 2012.

[32] C. Flynn and M. B. Rubin. Undesirable anisotropy in a discrete fiber bundle model of fibrous tissues. In G. S. Kassab and M. S. Sacks, editors, *Structure-Based Mechanics of Tissues and Organs*, pages 329–345. Springer US, 2016.

[33] P. J. Flory. Thermodynamic relations for highly elastic materials. *Trans. Faraday Soc.*, 57:829–838, 1961.

[34] R. W. Ogden. Nearly isochoric elastic deformations: Application to rubberlike solids. *J. Mech. Phys. Solids*, 26:37–57, 1978.

[35] K. Li, R. W. Ogden, and G. A. Holzapfel. Computational method for excluding fibers under compression in modeling soft fibrous solids. *Eur. J. Mech. A/Solids*, 57:178–193, 2016.

[36] R. L. Taylor. *FEAP – A Finite Element Analysis Program, Version 8.4 User Manual*. University of California at Berkeley, Berkeley, California, 2013.

[37] G. A. Holzapfel. *Nonlinear Solid Mechanics. A Continuum Approach for Engineering*. John Wiley & Sons, Chichester, 2000.

[38] H. Weisbecker, C. Viertler, D. M. Pierce, and G. A. Holzapfel. The role of elastin and collagen in the softening behavior of the human thoracic aortic media. *J. Biomech.*, 46: 1859–1865, 2013.

[39] J. Burkardt. Estimate integrals over spherical triangles. *people.sc.fsu.edu/~jburkardt/f_src/sphere_triangle_quad/sphere_triangle_quad*, 2010.

[40] R. M. Murray, Z. Li, and S. S. Sastry. *A Mathematical Introduction to Robotic Manipulation*. CRC Press, Boca Raton, FL, 1994.

[41] G. Y. Qiu and T. J. Pence. Remarks on the behavior of simple directionally reinforced incompressible nonlinearly elastic solids. *J. Elasticity*, 49:1–30, 1997.

[42] J. C. Simo and R. L. Taylor. Quasi-incompressible finite elasticity in principal stretches. Continuum basis and numerical algorithms. *Comput. Meth. Appl. Mech. Eng.*, 85:273–310, 1991.

[43] The MathWorks Inc., MATLAB R2016a, Natick, MA, USA, 2016.

[44] Wolfram Research, Inc., Mathematica, Version 11.0, Champaign, Illinois, 2016.

[45] G. A. Holzapfel and R. W. Ogden. On fiber dispersion models: exclusion of compressed fibers and spurious model comparisons. *J. Elasticity*, 129:49–68, 2017.

[46] P.-B. Badel and J.-B. Leblond. A note on integration schemes for the microplane model of the mechanical behaviour of concrete. *Commun. Numer. Methods Eng.*, 20:354–361, 2004.

[47] P. Gagarinov. SPHERETRI: a triangulation of a unit sphere based on Icosahedron face partitioning. *www.mathworks.com/matlabcentral/fileexchange/58453-spheretri*.